Received: 10 October 2023 | Revised: 7 November 2023 | Accepted: 21 November 2023

DOI: 10.1002/cey2.526

RESEARCH ARTICLE

CARBON ENERGY WILEY

Enabling built-in electric fields on rhenium-vacancy-rich heterojunction interfaces of transition-metal dichalcogenides for pH-universal efficient hydrogen and electric energy generation

Benzhi Wang[1,2] | **Lixia Wang**[1] | **Ji Hoon Lee**[3] | **Tayirjan Taylor Isimjan**[4] | **Hyung Mo Jeong**[2] | **Xiulin Yang**[1]

[1]Guangxi Key Laboratory of Low Carbon Energy Materials, School of Chemistry and Pharmaceutical Sciences, Guangxi Normal University, Guilin, People's Republic of China

[2]Department of Smart Fab. Technology, School of Mechanical Engineering, Sungkyunkwan University, Suwon, Republic of Korea

[3]School of Materials Science and Engineering, Kyungpook National University, Daegu, Republic of Korea

[4]Saudi Arabia Basic Industries Corporation (SABIC) at King Abdullah University of Science and Technology (KAUST), Thuwal, Saudi Arabia

Correspondence
Tayirjan Taylor Isimjan, Saudi Arabia Basic Industries Corporation (SABIC) at King Abdullah University of Science and Technology (KAUST), Thuwal 23955-6900, Saudi Arabia.
Email: isimjant@sabic.com

Hyung Mo Jeong, Department of Smart Fab. Technology, School of Mechanical Engineering, Sungkyunkwan University, Suwon 16419, Republic of Korea.
Email: hmjeong@skku.edu

Xiulin Yang, Guangxi Key Laboratory of Low Carbon Energy Materials, School of Chemistry and Pharmaceutical Sciences, Guangxi Normal University, Guilin 541004, People's Republic of China.
Email: xlyang@gxnu.edu.cn

Funding information
Guangxi Technology Base and Talent Subject, Grant/Award Number: GUIKE AD20297039; Natural Science Foundation of Guangxi Zhuang Autonomous Region, Grant/Award Number: 2021GXNSFAA076001; National Research Foundation of Korea, Grant/Award Numbers: NRF-2021R1A2C4001777,

Abstract

Most advanced hydrogen evolution reaction (HER) catalysts show high activity under alkaline conditions. However, the performance deteriorates at a natural and acidic pH, which is often problematic in practical applications. Herein, a rhenium (Re) sulfide–transition-metal dichalcogenide heterojunction catalyst with Re-rich vacancies (NiS_2-ReS_2-V) has been constructed. The optimized catalyst shows extraordinary electrocatalytic HER performance over a wide range of pH, with ultralow overpotentials of 42, 85, and 122 mV under alkaline, acidic, and neutral conditions, respectively. Moreover, the two-electrode system with NiS_2-ReS_2-V_1 as the cathode provides a voltage of 1.73 V at 500 mA cm^{-2}, superior to industrial systems. Besides, the open-circuit voltage of a single Zn–H_2O cell with NiS_2-ReS_2-V_1 as the cathode can reach an impressive 90.9% of the theoretical value, with a maximum power density of up to 31.6 mW cm^{-2}. Moreover, it shows remarkable stability, with sustained discharge for approximately 120 h at 10 mA cm^{-2}, significantly outperforming commercial Pt/C catalysts under the same conditions in all aspects. A series of systematic characterizations and theoretical calculations demonstrate that Re vacancies on the heterojunction interface would generate a stronger built-in electric field, which profoundly affects surface charge distribution and subsequently enhances HER performance.

NRF-2022M3H4A1A04096482, RS-2023-00229679; Project of High-Level Talents of Guangxi, Grant/Award Number: F-KA18015; National Natural Science Foundation of China, Grant/Award Numbers: 21965005, 52363028

KEYWORDS
built-in electric field, electrocatalysts, hydrogen evolution reaction, self-powered system, water splitting, Zn–H_2O cell

1 | INTRODUCTION

The continuously growing demand for fossil fuels in modern society has led to an energy crisis. Additionally, the excessive use of fossil fuels has accelerated global climate warming, posing significant challenges to the future development of humanity.[1] Therefore, the search for sustainable, clean, and renewable energy sources has garnered increasing attention. Hydrogen is the most promising green fuel to solve fossil fuel exhaustion owing to its high energy density and lack of harmful gas emissions (CO, CO_2, etc.).[2,3] Hydrogen production by water splitting and use of a zinc (Zn)–H_2O fuel cell with hydrogen evolution reaction (HER) at the cathode has attracted considerable attention because of the lack of pollution and greenhouse gas emissions.[4,5] HER catalysts, in particular, platinum (Pt)-based catalysts, are widely used in acidic media because the Pt–H bond is associated with fast kinetics,[6] but they are limited by the fact that they are not stable in nonacidic conditions. Moreover, their high cost and low reserves on earth limit their large-scale practical application.[7,8]

Consequently, the focus was shifted to non-precious-metal-based catalysts, but these are limited by acidic corrosion, low stability, and high overpotential and are typically much inferior to Pt-based catalysts. As the Pt alternative, rhenium (Re) has similar Re–H bond strength but has not been studied widely as a HER catalyst. Nevertheless, Re is still a noble metal with similar shortcomings as Pt, regardless of being cheaper than Pt. To overcome the high cost, combining Re with a non-precious-metal catalyst that has unique electrochemical properties and may synergize with Re compounds is logical. Therefore, earth-abundant transition-metal dichalcogenides (TMDs) could be the best candidate owing to their open frameworks and unique electrochemical properties.[9] Besides, as a 2D material, rhenium disulfide (ReS_2) forms a 1 T′ structure with triclinic symmetry.[10] The unique structural feature endows ReS_2 with many novel properties, such as unique anisotropy and weak interlayer coupling, promoting excellent electrocatalytic performance.[11,12] Moreover, 1 T′ ReS_2 shows strong stability under both acid/base conditions.[13] Most importantly, the combination of ReS_2 with TMDs may overcome the limitations of TMDs, including insufficient active sites, poor durability, and weak electrical conductivity.

In addition, recent studies have shown that heterostructure materials, especially nanoscale heterostructure materials, have tunable interfacial electrons in the heterojunction structure, resulting in a high number of active catalyst sites, conductivity, and stability due to a built-in electric field (BIEF) at the heterojunction interface.[14] The energy band difference between the two materials induces interfacial polarization, leading to a potential difference. This difference will drive directional electron transport near the interface until the Fermi levels on both sides are aligned.[15] The BIEF-derived electron transfer can significantly accumulate a higher concentration of reagent ions near the surface of the electrocatalyst, thereby improving the mass transfer and reducing the energy barrier of reaction intermediates to enhance the activity and selectivity of the catalyst.[16] Furthermore, the strength of the BIEF affects the charge redistribution on the interface, thereby affecting the kinetics of the HER.[17] Therefore, regulating the BIEF at the heterojunction interface could be a strategy worth considering to significantly improve the HER kinetics in electrocatalysts. Recent research has demonstrated that hetero-interface engineering, introduction of vacancies, and heteroatom doping are effective strategies for creating BIEFs within catalytic materials.[18] Hence, cation vacancies have attracted increasing research interest due to their different electron and orbital distributions, which can act as electron acceptors to effectively adjust the electronic and energy band structures of catalysts.[19] Therefore, introduction of metal vacancies at the heterostructure interface to regulate the strength of BIEF is a promising strategy. The enhanced BIEF can accelerate charge transfer, enabling faster adsorption and desorption of catalytic intermediates at the interface, resulting in higher catalytic activity (Figure 1A).

Herein, by introducing Re vacancies at the interface of the NiS_2-ReS_2 heterostructure (NiS_2-ReS_2-V), we have created a stronger BIEF, resulting in excellent electrocatalytic HER performance over a wider range of pH. Under alkaline, acidic, and neutral conditions, the optimized NiS_2-ReS_2-V_1 showed low overpotentials of 42, 85, and 122 mV, respectively. The industrialized two-

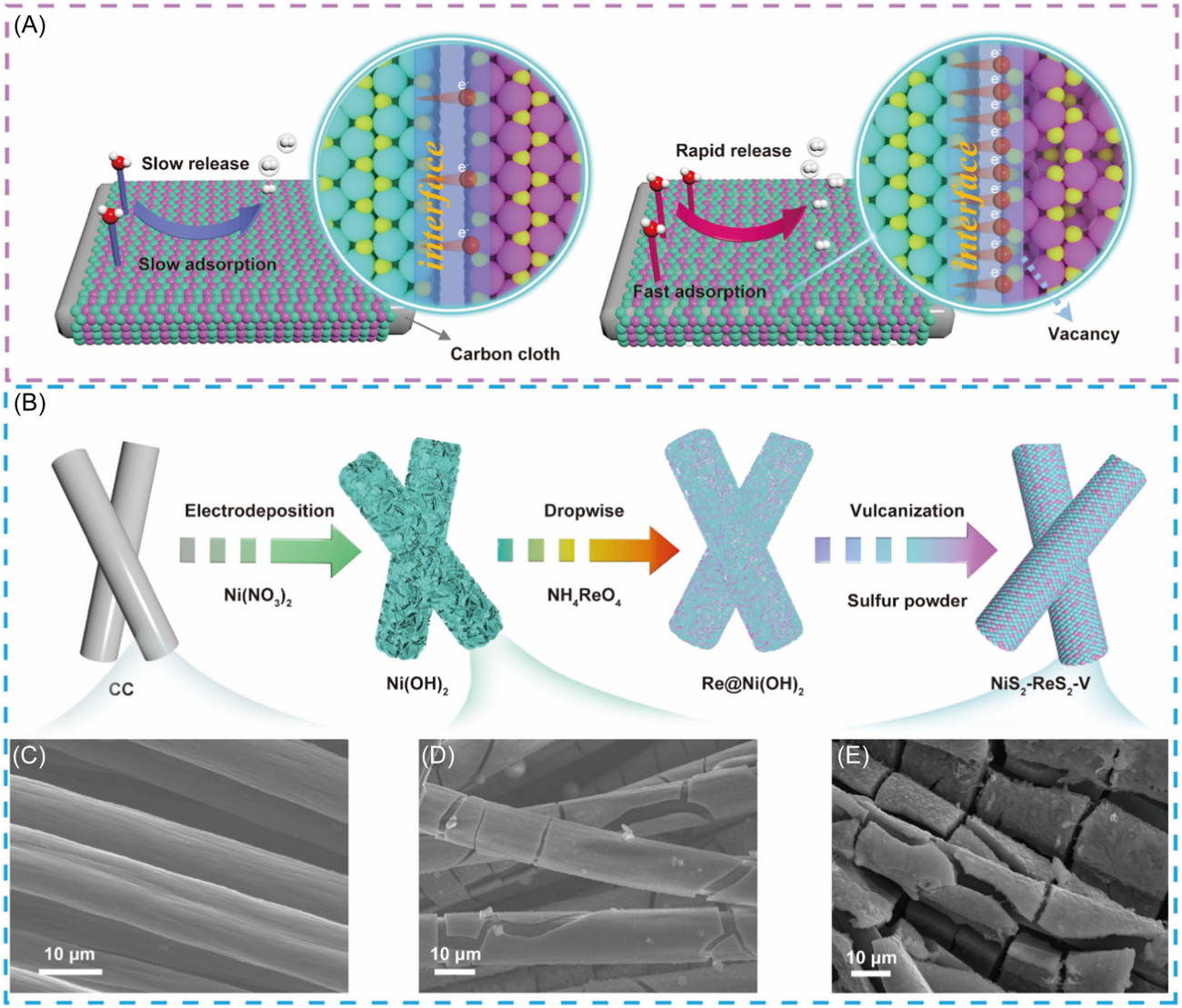

FIGURE 1 (A) Schematic illustration of charge redistribution under the regulation of the built-in electric field. (B) Schematic illustration of the synthesis of NiS_2-ReS_2-V. SEM images of (C) carbon cloth, (D) $Ni(OH)_2$, and (E) NiS_2-ReS_2-V_1.

electrode test revealed that high current densities of 500 and 1000 mA cm^{-2} could be achieved when the voltage was only 1.73 and 1.83 V, respectively. Moreover, the open-circuit voltage (OCV) of a Zn–H_2O cell can reach 90.9% along with a high-power density of 31.6 mW cm^{-2}. Both experiments and the theoretical analysis proved that NiS_2-ReS_2-V showed excellent HER over a wide range of pH, apart from its intrinsic property, mainly due to the generation of a stronger BIEF at the heterojunction interface caused by Re vacancies, thus promoting the charge redistribution. This enables reduction of ΔG_{H^*} and enhancement of electrical conductivity, thereby accelerating the HER kinetics. Our study provides a novel approach to improving HER performance by regulating the strength of the BIEF by introducing metal vacancies in heterostructures.

2 | EXPERIMENTAL SECTION

2.1 | Materials

Nickel nitrate hexahydrate ($Ni(NO_3)_2{\cdot}6H_2O$, ≥98%), ammonium perrhenate (NH_4ReO_4, >99.999%), sulfur powder (S), absolute ethanol (C_2H_5OH, ≥99.7%), Nafion (5% solution), ruthenium chloride hydrate ($RuCl_3{\cdot}xH_2O$, 99%), and potassium hydroxide (KOH) were purchased from Guangxi Zoey Biotechnology Co., Ltd. The commercial Pt/C (20 wt.% for platinum) was purchased from Alfa Aesar. Sulfuric acid (H_2SO_4, 95.0~98.0%), disodium phosphate hydrate ($Na_2HPO_4{\cdot}12H_2O$, >99.0%), and sodium dihydrogen phosphate ($NaH_2PO_4{\cdot}2H_2O$, >99.0%) were purchased from Xilong Chemical Co., Ltd. Zinc acetate dihydrate ($Zn(Ac)_2{\cdot}2H_2O$, ≥99.0%) was

purchased from Tianjin Masco Chemical Co., Ltd. Carbon cloth (CC WOS1009) was purchased from Taiwan CeTech. All reagents were analytical reagents and used as received without further purification.

2.2 | Synthesis of NiS_2, ReS_2, NiS_2-ReS_2, and NiS_2-ReS_2-V_x

NiS_2-ReS_2-V_x was prepared by coating 0.5 g of sulfur powder on a series of Ni–Re-species/CC surfaces, then slowly heated (3°C min^{-1}) to a certain temperature (200, 300, 400, or 500°C) in an Ar atmosphere (200 sccm) and maintained for 4.0 h, and finally cooled down to room temperature. After washing with deionized water and drying naturally, the materials prepared at 200, 300, 400, and 500°C were denoted as NiS_2-ReS_2, NiS_2-ReS_2-V_1 NiS_2-ReS_2-V_2, and NiS_2-ReS_2-V_3, respectively. For comparison, NiS_2 and ReS_2 were also prepared using a similar method, except for the addition of Re and Ni sources.

2.3 | Electrochemical measurements

The electrochemical performance of the as-prepared catalysts was investigated using an electrochemical workstation (VMP3, Biologic) with a typical three-electrode system in 0.5 M H_2SO_4, 1.0 M phosphate-buffered saline (PBS), and 1.0 M KOH electrolyte. A catalyst-modified CC, a graphite plate, and a saturated calomel electrode (SCE) were used as the working, counter, and reference electrodes, respectively. Cyclic voltammetry (CV) tests were carried out for five cycles to stabilize the electrocatalytic performance of the catalyst at a scan rate of 20 mV s^{-1}. Subsequently, linear sweep voltammetry (LSV) curves were obtained at a low scan rate of 5 mV s^{-1}, and electrochemical impedance spectroscopy (EIS) was performed near the onset potential over a frequency range of 200 kHz to 10 mHz. All potentials (vs. SCE) in this study were calibrated to the reversible hydrogen electrode (RHE) using the average CV curves of the two potentials at which the current crossed zero (0.232, 1.040, and 0.649 V). These values were considered thermodynamic potentials in hydrogen-saturated 0.5 M H_2SO_4, 1.0 M KOH, and 1.0 M PBS solution, respectively, as illustrated in Figure S11. All reported curves were corrected using the *i*R compensation. For the Zn–H_2O cell test, NiS_2-ReS_2-V_1 and a zinc sheet were used as the cathode and the anode, respectively. A mixed solution consisting of 0.6 M KOH and 0.2 M zinc acetate was used as an electrolyte. The polarization curve and OCV were obtained using an electrochemical workstation (CHI 760E). The stability of the Zn–H_2O cell was tested using a LAND cell testing system (BT2016A) at a current density of 10 mA cm^{-2}, and all electrochemical tests were performed at room temperature (25 ± 1°C).

2.4 | Computational method

The first-principle DFT calculations were performed by the Vienna Ab initio Simulation Package (VASP) using the projector-augmented wave (PAW) method. The exchange functional was treated using the generalized gradient approximation (GGA) of the Perdew–Burke–Ernzerhof (PBE) functional. The DFT + D3 method, developed by Grimme, was used to treat the van der Waals interactions. The energy cutoff for the plane-wave basis expansion was set to 500 eV, and the force on each atom less than 0.01 eV/Å was set for the convergence criterion of geometry relaxation. Self-consistent calculations applied a convergence energy threshold of 10^{-6} eV. The heterojunction model consists of monolayer ReS_2 and the (200) surface of cubic NiS_2 ($a = 5.6849$ Å). A vacuum of approximately 15 Å was added in the *z*-direction to avoid periodic interactions. Brillouin zone integration was performed using $2 \times 3 \times 1$ Monkhorst and Pack k-point sampling for all computational processes.

The HER reaction was as follows:

$$H_2O + e^- \rightarrow H^* + OH^-$$

$$* + H^+ + e^- \rightarrow *H \rightarrow * + 1/2H_2(g).$$

The asterisk (*) represents the surface substrate active sites. The equation was used to calculate the free energy of the HER step: $\Delta G = \Delta E_{DFT} + \Delta E_{ZPE} - T\Delta S$, where ΔE_{DFT} is the DFT electronic energy difference of each step; ΔE_{ZPE} and ΔS are the correction of the zero-point energy and variation of entropy, respectively, which are obtained using the vibration analysis; and T is the temperature (room temperature).

3 | RESULTS AND DISCUSSION

3.1 | Synthesis and characterization of electrocatalysts

The schematic diagram of the preparation of the NiS_2-ReS_2-V composite is shown in Figure 1B. First, carbon cloth (CC) with a clean surface that had been subjected to hydrophilic treatment was used as the substrate (Figure 1C. For more details, see the supporting information). Then, CC was used as the working

electrode to obtain $Ni(OH)_2$ composed of ultrathin nanosheets as the starting material through in situ electrodeposition, as shown in Figures 1D, S1, and S2, followed by the dropwise addition of ammonium perrhenate to $Ni(OH)_2$ to form $Re@Ni(OH)_2$. Finally, a composite material with Re vacancies (NiS_2-ReS_2-V) was successfully obtained by taking advantage of the heat treatment, which weakened the interlayer interaction of ReS_2, leading to the decoupling of lattice vibrations between layers of ReS_2 and generation of Re vacancies (Figure 1E).[20] It is well known that the concentration of defects in materials can be controlled by temperature.[21] Therefore, we prepared samples with varying defect concentrations by calcining the precursor at different temperatures (NiS_2-ReS_2-V_x; $x = 1$, 2, and 3; for more details, see the experimental section). The crystal structures of NiS_2, ReS_2, and NiS_2-ReS_2-V_x were investigated using powder X-ray powder diffraction (XRD). The samples completely coincided with the standard diffraction peaks of the triclinic crystal structure of NiS_2 (JCPDS No. 73-0574) and ReS_2 (JCPDS No. 82-1379), respectively, as presented in Figure S3A. In ReS_2, the characteristic diffraction peaks at 26.6° and 43.4° correspond to the (111) and (100) crystal planes of carbon, respectively. Moreover, as shown in Figure S3B, the complexes with different heat treatments show similar characteristic peaks, confirming the identical composition. Raman spectroscopy was used to examine changes in the energy band structure of the materials. In Figure S4, the peak at 476.5 cm^{-1} was attributed to the typical A_g mode of NiS_2.[22] Two prominent peaks appeared at approximately 149 and 210 cm^{-1}, corresponding to the in-plane (E_g) and out-of-plane (A_g) vibration modes of ReS_2, respectively.[23] These two peaks arise owing to the low crystal symmetry and association with fundamental Raman modes coupled to each other and acoustic phonons. The peaks at 275, 309, 402, and 438 cm^{-1} belong to the second-order peak of ReS_2.[24] The NiS_2-ReS_2-V_x composite was composed of vibration models of NiS_2 and ReS_2, which further proved that NiS_2-ReS_2-V_x was composed of NiS_2 and ReS_2. In addition, the Raman spectra of the composite material after vulcanization at different temperatures show similar vibrational patterns, further demonstrating that the complexes have the same composition, which is consistent with the XRD results presented in Figure S4. Additionally, the defect concentration in the material influences the catalytic activity during the HER process.[25] In this context, we chose NiS_2-ReS_2-V_1 with a moderate defect concentration for further characterization and analysis.

The morphologies and microstructures of the catalysts were systematically studied using scanning electron microscopy (SEM) and transmission electron microscopy (TEM). It can be seen that NiS_2-ReS_2-V_1 is a porous structure composed of numerous nanoparticles in situ-grown on carbon cloth, as illustrated in Figures 1E and 2A. This porous structure provides more exposed surfaces and abundant transport channels, promoting mass transfer during the catalytic process. The TEM image in Figure 2B further demonstrates that NiS_2-ReS_2-V_1 was composed of nanoparticles with an average size of approximately 9.2 nm (Figure 2B inset). High-angle annular dark-field (HAADF) TEM results demonstrated the presence of Re, Ni, and S, which were uniformly distributed in NiS_2-ReS_2-V_1, as shown in Figure 2C. Low-magnification high-resolution TEM (HRTEM) images reveal the presence of curved layered structures and numerous interfaces. These curved structures may be attributed to the thermal bending effect of ReS_2 and the bending of the lattice plane caused by vacancies (Figure 2D).[26] The enlarged HRTEM clearly shows the lattice orientation and interface, demonstrating the successful construction of the heterostructure, as presented in Figure 2E. The characteristic lattice fringe of 0.28 nm can correspond to the (200) crystal plane of NiS_2 in the NiS_2-ReS_2-V_1 heterostructure.[27] The selected area electron diffraction (SAED) pattern shows that NiS_2-ReS_2-V_1 has a ring pattern with a polycrystalline nature. The five stronger rings are assigned to the (200), $(0\bar{1}2)$, $(\bar{1}\,\bar{1}2)$, $(\bar{2}02)$ crystal planes of ReS_2 and the (310) crystal plane of NiS_2, respectively, as displayed in Figure 2F. This further proves the success of heterostructure construction. In addition, a typical layered structure with a layer spacing of 6.2 Å can be observed in the HRTEM image of the curved edge; this space was slightly larger than the interlayer spacing of 6.1 Å bulk ReS_2.[28] Notably, the lattice fringes along the curled edge were discontinuous. Additionally, many dislocations and distortions can be identified, attributed to the rich vacancies.[29] The N_2 absorption–desorption isotherms of NiS_2-ReS_2 and NiS_2-ReS_2-V_1 at 77 K both show a hysteresis loop with typical type IV isotherms (Figure 2G), confirming the presence of mesopores.[30] The BJH pore-size distributions of NiS_2-ReS_2 and NiS_2-ReS_2-V_1 show a mesoporous structure with a pore size of 3.8 nm (Figure 2H). The rich mesoporous structure is conducive to the mass transfer process of HER, which is consistent with the results of SEM and TEM. It is worth noting that NiS_2-ReS_2-V_1 shows a larger Brunauer–Emmett–Teller (BET) specific surface area (22.01 $m^2\,g^{-1}$) and pore volume (0.028 $cm^3\,g^{-1}$) compared with NiS_2-ReS_2 (6.58 $m^2\,g^{-1}$ and 0.009 $cm^3\,g^{-1}$). This porous structure is attributed to the generation of vacancies during the heat-treatment process.[31]

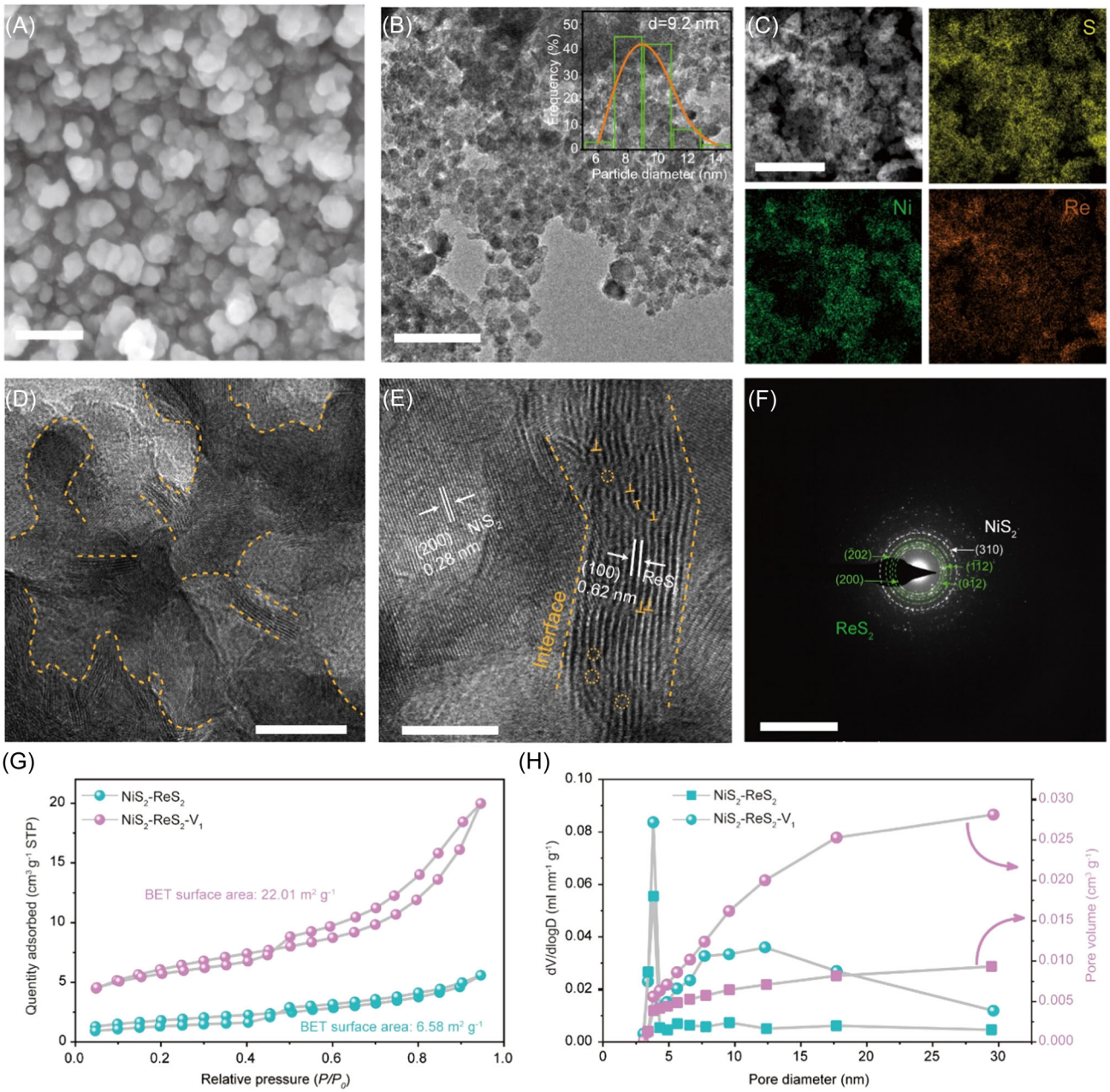

FIGURE 2 (A) SEM image of NiS_2-ReS_2-V_1. The scale bar indicates 2 μm. (B) TEM image of NiS_2-ReS_2-V_1 with particle size distribution (inset). The scale bar indicates 100 nm. (C) HAADF-TEM and elemental mapping of NiS_2-ReS_2-V_1. The scale bar indicates 200 nm. (D) HRTEM image of NiS_2-ReS_2-V_1. The generated interfaces are marked by yellow dashed lines. The scale bar indicates 20 nm. (E) Lattice orientation and interface of NiS_2-ReS_2-V_1. The line defects and vacancies are marked by yellow symbols. The scale bar indicates 10 nm. (F) SAED pattern of NiS_2-ReS_2-V_1. The diffraction patterns in green and white colors indicate ReS_2 and NiS_2 in NiS_2-ReS_2-V_1, respectively. The scale bar indicates 10 1/nm. (G) Nitrogen adsorption–desorption isotherms and (H) pore size distribution of NiS_2-ReS_2 and NiS_2-ReS_2-V_1.

3.2 | Effect of Re vacancies in enhancing BIEF on heterojunction interfaces

Electron paramagnetic resonance (EPR) spectroscopy was used to demonstrate that the catalyst has vacancies. As shown in Figure 3A, no significant EPR signal was observed in NiS_2-ReS_2. In contrast, NiS_2-ReS_2-V_1 shows a strong peak, and importantly, the intensity of these peaks increases with increasing temperature. This indicates that more vacancies will be generated as the temperature increases. Positron annihilation lifetime spectra (PALS) were used to study the type and relative concentration of cation vacancies due to its nondestructive and selective detection of negatively charged defects in solid materials with ppm-level sensitivity.[32] In the PALS shown in

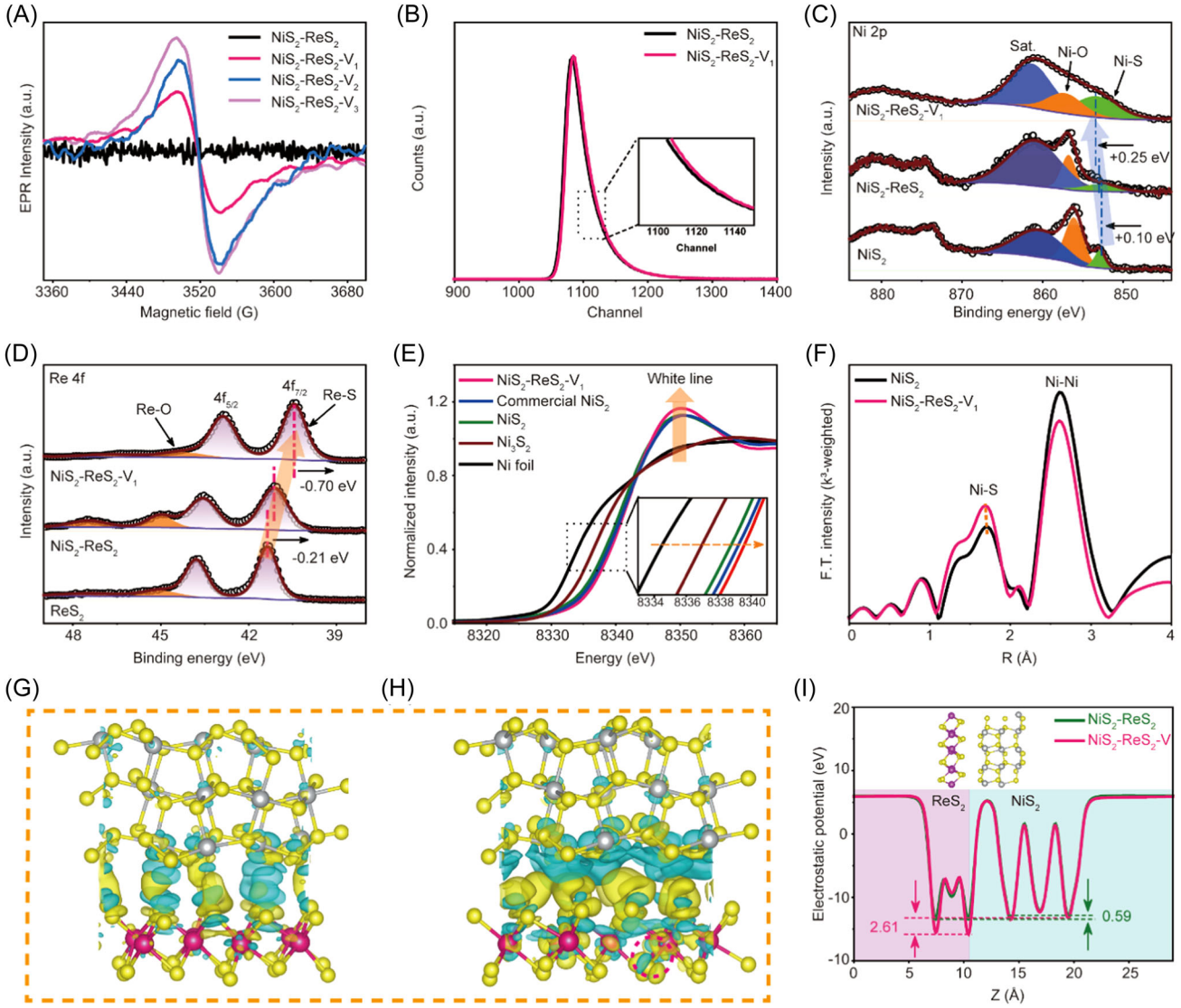

FIGURE 3 (A) EPR patterns of NiS_2-ReS_2, NiS_2-ReS_2-V_1, NiS_2-ReS_2-V_2, and NiS_2-ReS_2-V_3. (B) PALS of NiS_2-ReS_2 and NiS_2-ReS_2-V_1. (C) High-resolution XPS of Ni 2*p* and (D) Re 4*f* of NiS_2, ReS_2, NiS_2-ReS_2, and NiS_2-ReS_2-V_1. (E) XANES spectra of the Ni K-edge for NiS_2-ReS_2-V_1, NiS_2, Ni foil, commercial NiS_2, and Ni_3S_2. (F) EXAFS spectra of the Ni K-edge for NiS_2-ReS_2-V_1 and NiS_2. (G) Charge-density difference diagram of NiS_2-ReS_2 and (H) NiS_2-ReS_2-V. The isosurface value is 0.002 e/Å^3. (I) Plane-averaged electronic potential along the perpendicular direction of NiS_2-ReS_2 and NiS_2-ReS_2-V.

Figure 3B, NiS_2-ReS_2-V_1 shows a larger full-width at half-maximum (FWHM) compared with NiS_2-ReS_2. Typically, a larger FWHM indicates a greater number of defects. Furthermore, on the basis of the corresponding derived lifetime parameters shown in Table S1, all samples display two distinct lifetime components (τ_1 and τ_2). The shortest one, τ_1 (≈357 ps), could be ascribed to the bulk lifetime. The most extended lifetime τ_2 components could be attributed to positron annihilation in the more significant size defect.[33] Since larger defects have lower average electron density than small ones, resulting in a lower annihilation rate and thus increased positron lifetime.[34] Therefore, NiS_2-ReS_2-V_1 has more defects than NiS_2-ReS_2. The mean lifetime (τ_m) describes the properties of overall positron annihilation of samples. The small τ_m value of NiS_2-ReS_2-V_1 further indicates the presence of more defects. Inductively coupled plasma atomic emission spectrometry (ICP-AES) was used to analyze the mass fractions of Re and Ni in catalysts calcined at different temperatures (Figure S5). The Re content decreased with increasing calcination temperature, while the change in the Ni content was negligible. The results confirmed that high temperature facilitates the formation of Re vacancies, which is consistent with the EPR, PALS, and HRTEM results, as presented in Figure S5 and Table S2.

X-ray photoelectron spectroscopy (XPS) was performed to characterize the elemental composition and surface chemical valence states of NiS_2, ReS_2, NiS_2-ReS_2, and NiS_2-ReS_2-V_1. First, the binding energies were corrected using C 1*s* as the standard, as shown in Figure S6A. Subsequently, the XPS survey and high-resolution spectra were analyzed. The XPS survey confirmed the presence of Ni, Re, S, and O in NiS_2-ReS_2-V_1, as presented in Figure S6B. The high-resolution Ni 2*p* spectra of NiS_2, NiS_2-ReS_2, and NiS_2-ReS_2-V_1 are shown in Figure 3C, which can be deconvoluted into three subpeaks in NiS_2-ReS_2-V_1, corresponding to Ni–S (853.24 eV), Ni–O (857.25 eV), and satellite peaks.[35,36] Two different spin–orbit peaks can be observed in the high-resolution Re 4*f* spectrum of NiS_2-ReS_2-V_1, which indicates that Re exists in two other valence states in the complex, as shown in Figure 3D. The peaks at 40.44 and 42.87 eV were assigned to the Re–S bond,[37] while 44.24 and 46.67 eV corresponded to the oxidized Re species.[38] Figure S7 shows the high-resolution S 2*p* spectrum of NiS_2-ReS_2-V_1. The located at 160.93 and 162.09 eV belong to the S $2p_{3/2}$ and S $2p_{1/2}$ of metal sulfides (ReS_2 and NiS_2),[39] while 167.92 and 169.47 eV were assigned to sulfur oxides, which may be related to the oxidation of sulfur in the air.[40] Remarkably, compared with single NiS_2 and ReS_2, the binding energy of the Ni–S bond in NiS_2-ReS_2 and NiS_2-ReS_2-V_1 is positively shifted by 0.1 and 0.25 eV, while the binding energy of the Re–S bond is negatively shift by 0.21 and 0.70 eV. This result confirmed interface contact and electron transfer from NiS_2 to ReS_2 in the NiS_2-ReS_2 heterojunction structure. In addition, the larger binding energy shift in NiS_2-ReS_2-V_1 evidenced a stronger BIEF at its interface.[41]

In addition, X-ray absorption fine structure (XAFS) was used to gain further insight into the structural and electronic properties of the heterojunction interface. Figure 3E shows the Ni K-edge X-ray absorption near-edge structure (XANES) spectra of NiS_2, NiS_2-ReS_2-V_1, Ni foil, commercial NiS_2, and Ni_3S_2. NiS_2 and NiS_2-ReS_2-V_1 showed XANES curves similar to those of commercial NiS_2, but differed from those of Ni foil and Ni_3S_2, proving that Ni in NiS_2 and NiS_2-ReS_2-V_1 has a similar coordination environment to commercial NiS_2. Interestingly, the absorption edge of NiS_2-ReS_2-V_1 slightly shifts to higher energies than that of NiS_2, which demonstrates that Ni donates electrons to Re in NiS_2-ReS_2-V_1.[42] In addition, the prominent peak of the Ni K-edge, historically known as the white line, corresponds to the electronic transition from the occupied 1*s* orbital to the partially unoccupied 4*p* orbital.[43] According to the existing studies, the magnitude of the integrated intensity of the white line is proportional to the density of unoccupied orbitals.[44] The white line of NiS_2-ReS_2-V_1 shows a slightly higher peak intensity than that of NiS_2, confirming electron density changes around Ni at the heterojunction interface.[45] This result was consistent with the XPS results. The extended X-ray absorption fine structure (EXAFS) analysis was performed to further explore the coordination environment of Ni in the catalyst. The Fourier transform (FT) k^3-weighted EXAFS spectra of NiS_2 yielded two main peaks, as shown in Figure 3F. The peak located at 1.71 Å corresponds to the first coordination shell of Ni–S[46] and the peak at 2.61 Å corresponds to the second coordination shell of Ni–Ni. Moreover, Ni–S in NiS_2-ReS_2-V_1 presents a slight shift (1.68 Å) compared with NiS_2, which was attributed to the modulation of the coordination environment for Ni atoms by ReS_2.

The effect of Re vacancies on the charge redistribution on heterojunction interfaces was further investigated through first-principles calculations. First, the NiS_2-ReS_2 heterogeneous structure was optimized to obtain a stable form with a lower energy as a study model, as shown in Figure S8. The charge-density difference diagram was used to investigate the origin of charge transfer at the heterojunction interface. The charge-density difference diagrams of NiS_2-ReS_2 and NiS_2-ReS_2-V are displayed in Figure 3G-H. The charge depletion on NiS_2 and accumulation on ReS_2 can be clearly observed. Interestingly, there is more charge depletion and accumulation on NiS_2 and ReS_2 in NiS_2-ReS_2-V compared to NiS_2-ReS_2, suggesting more electron transfer from NiS_2 to ReS_2 at the heterojunction interface.[47] Simultaneously, the charge transfer in the heterojunction is interpreted more accurately according to Bader's charge analysis.[48] Calculation results show that a net 0.03 e^- were transferred in NiS_2-ReS_2, while 0.15 e^- were transferred in NiS_2-ReS_2-V, as shown in Table S3. This result further proved that introducing Re vacancies promotes the charge redistribution at the heterojunction interface. Density of states (DOS) was calculated to explore the modulation of the local electronic structure of the heterojunction by introducing Re vacancies.[49] The DOS diagrams are shown in Figure S9. NiS_2-ReS_2-V showed a higher occupation state near the Fermi level than NiS_2-ReS_2, NiS_2, and ReS_2, which revealed that the introduction of Re vacancies promoted electron transfer and enhanced the conductivity of catalysts.[50] More insight into the effect of Re vacancies in heterostructure is gained by analyzing the electrostatic potential distribution. The planar averaged self-consistent electrostatic potential for the NiS_2-ReS_2 and NiS_2-ReS_2-V heterostructures as a function of position in the z-direction is presented in Figure 3I. On the left and right are ReS_2 and NiS_2, respectively, as shown in the inset. After introducing Re vacancies, the potential difference between the S atomic layer in ReS_2

and the NiS_2 plane increases from the original 0.59 to 2.61 eV. The large potential difference implies a stronger BIEF at the heterojunction interface with Re vacancies,[51] and the results are consistent with those of XPS and XAFS analyses, as presented in Figure 3C–F. Accordingly, the main trend can be determined following experiments and theoretical calculations: when NiS_2 and ReS_2 are coupled to each other, a BIEF is formed at the interface, driving electrons to flow from NiS_2 to ReS_2 until the system reaches the same Fermi level. More importantly, on introducing Re vacancies into the heterojunction, a stronger BIEF would be formed, and more electrons would flow from NiS_2 to ReS_2. Therefore, the interfacial charge distribution can be more effectively controlled.

3.3 | Electrochemical HER performance

The HER electrocatalytic activity of NiS_2-ReS_2-V was optimized by changing the calcination temperature and the amount of NH_4ReO_4. When 1 mmol NH_4ReO_4 and a calcination temperature of 300°C were used, the catalyst (NiS_2-ReS_2-V_1) showed the best HER activity and the smallest electrochemical impedance, as shown in Figure S10. All potentials (vs. SCE) in this study were calibrated to the reversible hydrogen electrode (RHE) using the average CV curves of the two potentials at which the current crossed zero (Figure S11). All reported curves were corrected using the 100% *i*R compensation (Figure S12). The electrocatalytic performances of the optimized NiS_2-ReS_2-V_1 and control samples were first studied in 1.0 M KOH, as illustrated in Figure 4A. NiS_2-ReS_2-V_1 presented excellent activity, with a small overpotential of 42 mV at a geometric current density of $-10\ mA\ cm^{-2}$, which was lower than those of the control samples and Pt/C. In addition, NiS_2-ReS_2-V_1 showed a competitive electrocatalytic performance compared to previously reported non-noble metal catalysts, as presented in Table S4. Moreover, HER activities of the catalysts under acidic and neutral conditions were studied (Figure S13). NiS_2-ReS_2-V_1 showed 85 and 122 mV overpotentials at a geometric current density of $-10\ mA\ cm^{-2}$ in 0.5 M H_2SO_4 and 1.0 M PBS, respectively. These values were significantly lower than those of the control NiS_2, ReS_2, and many other transition-metal catalysts, as presented in Tables S5 and S6.

The Tafel slope can be used to evaluate the rate-determination steps in HER.[52] As can be observed from Figure 4B, the Tafel slope of NiS_2-ReS_2-V_1 was 84.8 mV dec^{-1}, indicating that the Volmer–Heyrovsky pathway is a rate-determining step in the alkaline solution.[53] Furthermore, the exchange current density (j_0) of an electrocatalyst can reflect its intrinsic catalytic activity under equilibrium conditions, which can normally be determined by extrapolating the Tafel slope to 0 V versus RHE. As shown in Figure 4C, NiS_2-ReS_2-V_1 demonstrated a large j_0 of $3.24\ mA\ cm^{-2}$, outperforming those of NiS_2-ReS_2 ($0.75\ mA\ cm^{-2}$), NiS_2 ($0.04\ mA\ cm^{-2}$), ReS_2 ($0.37\ mA\ cm^{-2}$), and Pt/C ($1.59\ mA\ cm^{-2}$), indicating a higher HER intrinsic catalytic activity.

Additionally, the electrochemical active surface areas (ECSAs) were calculated to explore the electrocatalytic activity (for details, see the Supporting Information). In general, ECSA is linearly proportional to the double-layer capacitance (C_{dl}).[54] The C_{dl} value can be determined from the current response in the capacitive region of the cyclic voltammetry (CV) curve at different scanning speeds in the non-Faradaic region (Figure S14) using a unit capacitance ($60\ \mu F\ cm^{-2}$).[55] As shown in Figure 4D, the measured C_{dl} of NiS_2-ReS_2-V_1 was $418.7\ mF\ cm^{-2}$, which was significantly higher than those of NiS_2-ReS_2 ($314.7\ mF\ cm^{-2}$), NiS_2 ($223.8\ mF\ cm^{-2}$), and ReS_2 ($167.3\ mF\ cm^{-2}$), demonstrating that NiS_2-ReS_2-V_1 has a larger ECSA. This can provide more catalytically active sites in the catalytic process. The ECSA-normalized current density curves of different catalysts confirm the excellent intrinsic catalytic activity of NiS_2-ReS_2-V_1, as shown in Figure 4E. According to the Nyquist plot in Figure S15, the smallest charge-transfer resistance of NiS_2-ReS_2-V_1 among the samples indicates the significant role of Re vacancies in enhancing the intrinsic electrocatalytic activity.[56]

Turnover frequency (TOF) is another significant parameter for assessing the inherent electrocatalytic activity of HER catalysts,[57] which can reflect the number of hydrogen molecules produced per second from each active site. Moreover, Figure 4F demonstrates that the TOF value of NiS_2-ReS_2-V_1 rapidly increases with increasing applied potential under acidic, alkaline, and neutral conditions. At the overpotential of −100 mV, TOF values of NiS_2-ReS_2-V_1 were 0.49, 0.19, and $1.35\ s^{-1}$ in acid, neutral, and alkaline conditions, respectively. In particular, under alkaline conditions, TOF was higher than that of most previously reported catalysts, as presented in Figure 4G and Table S7. The high TOF value indicates that NiS_2-ReS_2-V_1 can effectively promote the reaction under various conditions, which is the inherent reason for steady HER performance at a wide range of pH. The stability of the catalyst was evaluated using chronoamperometry (CP), as shown in Figure 4H. At a current density of $-100\ mA\ cm^{-2}$, NiS_2-ReS_2-V_1 presented excellent HER catalytic stability, maintained at 96%, 90%, and 97.9% after 24 h of testing under acidic, neutral, and alkaline conditions, respectively.

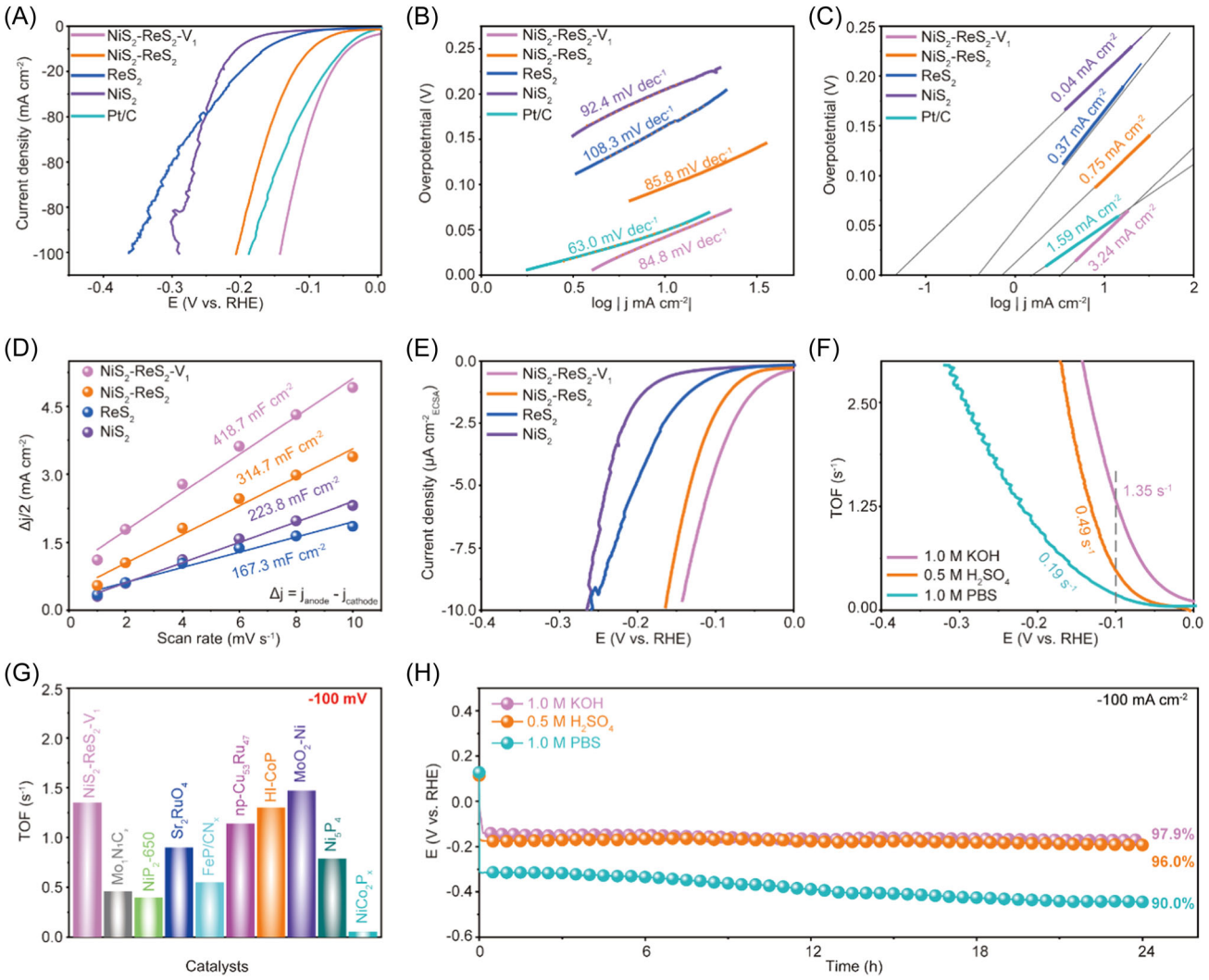

FIGURE 4 (A) LSV curves and (B) Tafel slopes of each electrocatalyst. (C) Exchange current density of each electrocatalysts. (D) Double-layer capacitance derived from ECSAs of each electrocatalysts. (E) ECSA-normalized current density curves of NiS_2, ReS_2, NiS_2-ReS_2, and NiS_2-ReS_2-V_1. (F) TOF curves of NiS_2-ReS_2-V_1 in different pH conditions. (G) Comparison of the TOF values with previously reported representative catalysts. (H) Durability tests of NiS_2-ReS_2-V_1 at a current density of $-100\ mA\ cm^{-2}$ under different pH conditions.

3.4 | Active site exploration for HER enhancement mechanism

To gain deeper insight into the active sites in the NiS_2-ReS_2-V_1 heterojunction, in situ Raman was used to elucidate the real-time surface structural variation of NiS_2-ReS_2-V_1 during the HER in 1.0 M KOH using the specially designed setup shown in Figure 5A. As shown in Figure 5B, at the OCV potential, the Raman characteristic peaks are consistent with the previous dry sample analysis results (Figure S4), mainly belonging to Re–S and Ni–S vibrations. When the potential is applied, two new characteristic Raman peaks appear at 475 and 526 cm^{-1}, and their peak intensities increase with increasing operating potential. These two peaks can be assigned to the E_g Ni–O bending and A_g Ni–O stretching vibrations.[9,58] The generation of the Ni–O vibration peak can be attributed to the adsorption and dissociation of water on nickel sites. This result implies that in the NiS_2-ReS_2-V_1 heterostructure, Ni serves as the genuine active site for alkaline HER.

First-principle calculations were carried out to further explore the working mechanism of Re vacancies on HER performance. Typically, HER in an alkaline solution involves water adsorption/dissociation, formation of adsorbed hydrogen intermediates ($H_2O + e^- \rightarrow H^* + OH^-$), and hydrogen generation ($H^* + H^+ + e^- \rightarrow 1/2H_2$).[59] For an alkaline HER, water dissociation is generally considered as the rate-determining step.[60] According to Figure 4B, the Tafel analysis suggests that the overall HER is based on the Volmer–Heyrovsky pathway. Figures S16–S19 show the optimized

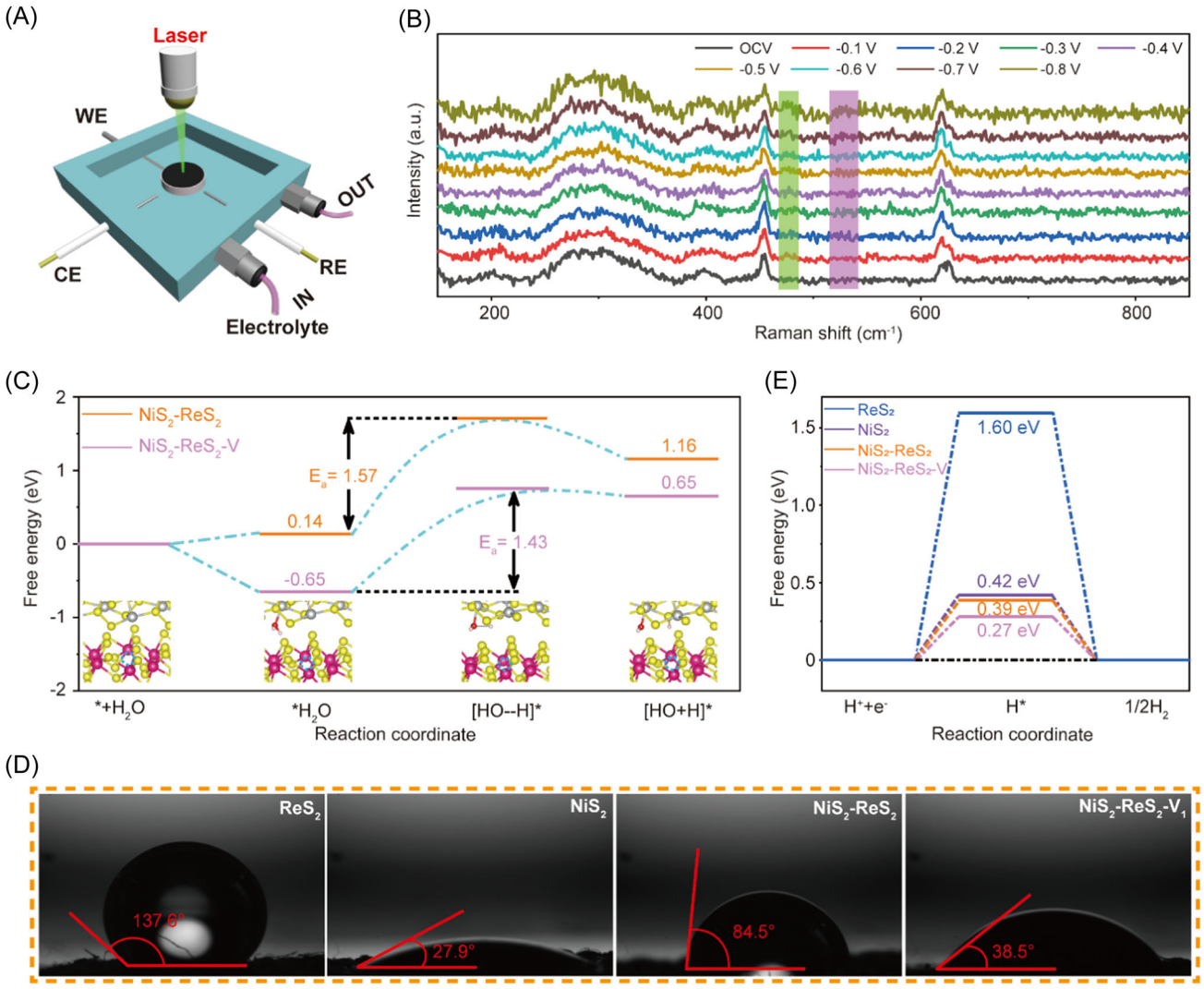

FIGURE 5 (A) Schematic diagram of the in situ Raman electrolyzer. (B) *In situ* Raman spectra of NiS_2-ReS_2-V_1 at varied potentials during HER in 1.0 M KOH. (C) Relative energy profiles and simplified surface structures of various reaction species along the alkaline Volmer reaction pathway of NiS_2-ReS_2 and NiS_2-ReS_2-V. (D) Contact angle image for NiS_2, ReS_2, NiS_2-ReS_2, and NiS_2-ReS_2-V_1. (E) Hydrogen adsorption free-energy diagrams of ReS_2, NiS_2, NiS_2-ReS_2, and NiS_2-ReS_2-V.

configuration for water adsorption/desorption on the catalyst. As shown in Figure 5C and S20, NiS_2-ReS_2-V has the lowest and most favorable water adsorption free energy ($\Delta E_{H2O*} = -0.65$ eV) compared to NiS_2 (−0.24 eV), ReS_2 (0.09 eV), and NiS_2-ReS_2 (0.14 eV), suggesting the highest ability to adsorb H_2O molecules, and thus a more efficient Volmer step to promote the HER reaction.[61] In particular, the activation energy of water dissociation to form an adsorbed H in NiS_2-ReS_2-V (1.43 eV) is lower than those of other control samples, indicating that the introduction of Re vacancies readily activates water molecules and accelerates water dissociation kinetics.[62] The wettability measurements in Figure 5D also indicate that the introduction of Re vacancies facilitates the adsorption of water molecules because NiS_2-ReS_2-V_1 shows a smaller contact angle (CA) compared to NiS_2-ReS_2, which benefits from the stronger BIEF at the heterostructure interface.[63] The free energy of H adsorption (ΔG_{H*}) is another key descriptor for evaluating the HER performance of electrocatalysts. In general, a Gibbs free energy close to zero is beneficial for balancing protons' adsorption and desorption rates on the active sites in HER.[2] Figure 5E shows the ΔG_{H*} sites on different catalysts. The results revealed that ΔG_{H*} values of ReS_2 and NiS_2 were 1.60 and 0.42 eV, while the ΔG_{H*} value of the pristine NiS_2-ReS_2 heterojunction was 0.39 eV, which was further reduced to 0.27 eV after introducing Re vacancies. Consequently, the introduction of Re vacancies in the heterojunction of NiS_2-ReS_2 is an efficient method for enhancing HER under universal pH conditions.

3.5 | Construction of a self-powered water-splitting system

High-purity hydrogen can be produced by conventional electrocatalytic water splitting and metal oxidation fuel cells, such as Zn–H_2O fuel cells, in which the conversion of chemical energy in Zn metal into electricity is accompanied by hydrogen production. As shown in Figure 6A, a coupling configuration between a Zn–H_2O cell and a hydrolyzer was established for the self-powered joint production of hydrogen by a fuel cell and electrocatalytic water splitting using NiS_2-ReS_2-V_1 as a cathode. The Zn–H_2O fuel cell is used as a chemical energy conversion device to perform HER and power generation simultaneously, and the generated electricity is used to drive water electrolysis. A single Zn–H_2O cell of NiS_2-ReS_2-V_1 showed an OCV of 1.2 V, achieving an

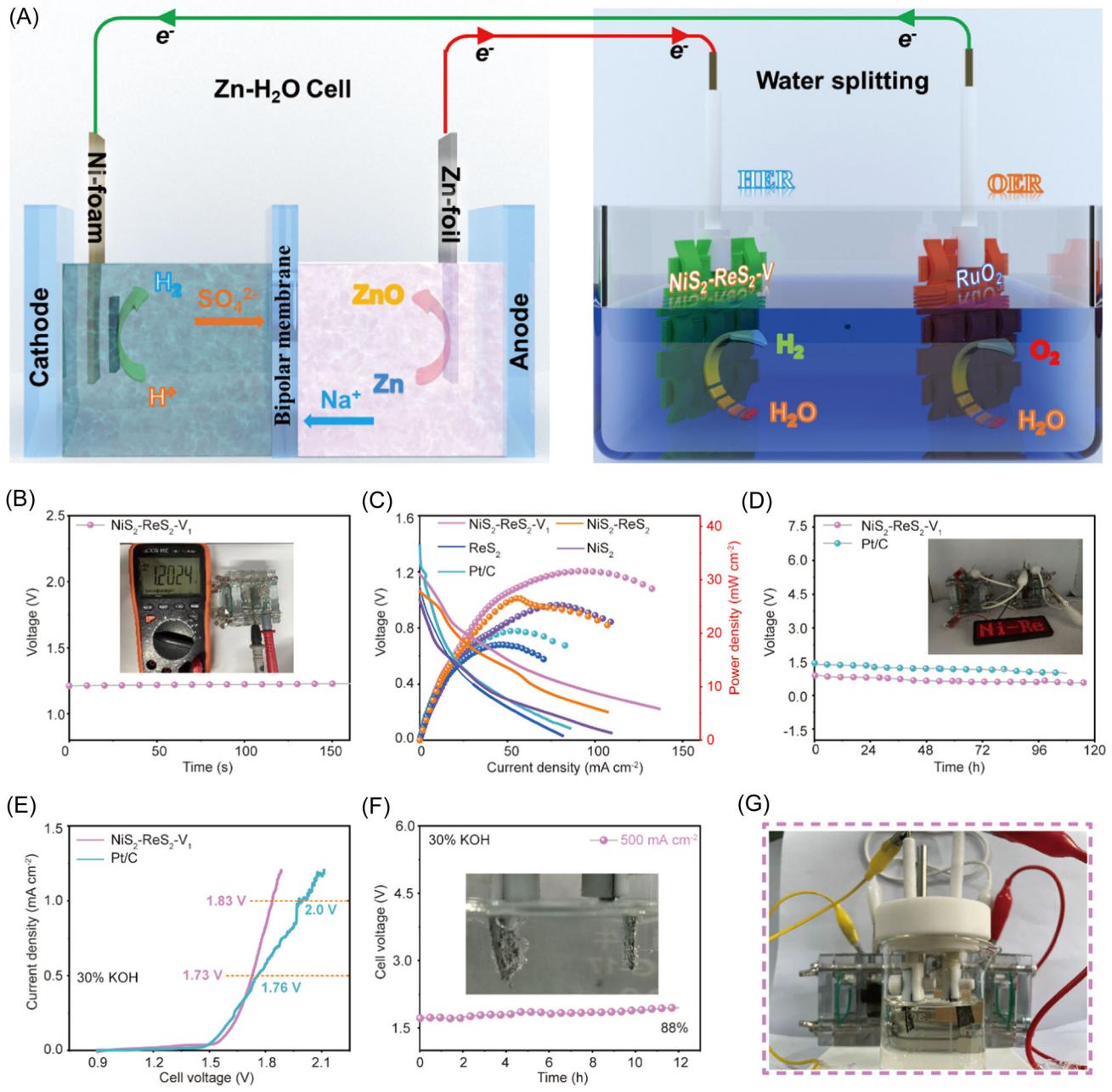

FIGURE 6 (A) Schematic illustration of the coupled configuration of Zn–H_2O cells driving electrocatalytic water splitting. (B) OCV plots of NiS_2-ReS_2-V_1. (C) Discharge polarization curves and the corresponding power densities of NiS_2-ReS_2-V_1, NiS_2-ReS_2, NiS_2, ReS_2, and Pt/C. (D) Long-term durability of NiS_2-ReS_2-V_1 and Pt/C. (E) Comparison of the water-splitting activity of $RuO_2^{(+)}$||NiS_2-ReS_2-$V_1^{(-)}$ versus $RuO_2^{(+)}$||$Pt/C^{(-)}$ in 30 wt.% KOH. (F) Long-term cycling tests of $RuO_2^{(+)}$||NiS_2-ReS_2-$V_1^{(-)}$ at high current densities in 30 wt.% KOH. (G) Digital photograph of the self-powered water-splitting system by double Zn–H_2O fuel cells in series.

impressive 90.9% of the theoretical voltage for the Zn–H_2O cell (1.32 V; for details, see the Supporting Information), which significantly surpasses the performance of the control catalysts, as shown in Figure 6B and S21A. In addition, Figure 6C shows that the maximum power density of NiS_2-ReS_2-V_1 was 31.6 mW cm^{-2} at a current density of 94.2 mA cm^{-2}, which was also superior to that of the control catalysts. Furthermore, the NiS_2-ReS_2-V_1-based cell could be discharged for approximately 120 h at a current density of 10 mA cm^{-2}, which was longer than that of commercial Pt/C and all other compared catalysts, as shown in Figures 6D and S21B. To further explore the potential application of the device, two NiS_2-ReS_2-V_1-based Zn–H_2O cells connected in series were used to illuminate a red LED board for power supply, as shown in the inset of Figure 6D.

To meet the requirements for the industrialization of catalysts, the optimized HER catalyst was combined with RuO_2 to form a two-electrode system ($RuO_2^{(+)}$||NiS_2-ReS_2-$V_1^{(-)}$). A high current density test was performed under industrial conditions (30 wt.% KOH). Figure 6E shows the steady-state potential polarization curve; the cell voltage required for $RuO_2^{(+)}$||NiS_2-ReS_2-$V_1^{(-)}$ at a low current density was slightly higher than that of $RuO_2^{(+)}$||$Pt/C^{(-)}$ for water splitting. However, with increasing applied voltage, $RuO_2^{(+)}$||NiS_2-ReS_2-$V_1^{(-)}$ provides a voltage of 1.73 V at a current density of 500 mA cm^{-2}, which is superior to those of commercial $RuO_2^{(+)}$||$Pt/C^{(-)}$ (1.76 V) and existing industrial systems (200~400 mA cm^{-2} at 1.8~2.4 V).[64] In addition, it only requires an additional 0.1 V voltage to increase the current density from 500 to 1,000 mA cm^{-2}. $RuO_2^{(+)}$||NiS_2-ReS_2-$V_1^{(-)}$ was superior to the previously reported catalysts at a current density of 100 mA cm^{-2} under alkaline condition, as presented in Table S8. As shown in Figure 6F, the NiS_2-ReS_2-V_1 catalyst maintained 88% of its catalytic activity after 12 h of continuous operation at a constant current density of 500 mA cm^{-2} in 30 wt.% KOH, and hydrogen and oxygen were generated violently during the reaction (inset of Figure 6F and Video S1), indicating significant durability and potential for use in industrial applications. Furthermore, NiS_2-ReS_2-V_1 was used as the cathode in both Zn–H_2O cells and a hydrolyzer to establish a self-powered system for electrocatalytic water splitting. The system can not only coproduce hydrogen from the fuel cells and water splitting but also simultaneously generate electricity to drive water splitting, as shown in Figure 6G.

4 | CONCLUSIONS

In this study, we present a simple synthetic strategy to introduce Re vacancies in the NiS_2-ReS_2 heterojunction interface (NiS_2-ReS_2-V). The optimized NiS_2-ReS_2-V_1 catalyst presents remarkable electrocatalytic HER performance, with ultra-low overpotentials of 42, 85, and 122 mV under alkaline, acidic, and neutral conditions, respectively. Moreover, NiS_2-ReS_2-V_1 is used in a self-powered system comprising Zn–H_2O cells and electrolytic water splitting, achieving impressive theoretical voltage efficiencies of up to 90.9%. Comprehensive characterizations and DFT theoretical calculations confirm that the excellent performance of the catalyst can be mainly attributed to the introduction of Re vacancies in the heterojunction, which creates a stronger built-in electric field at the interface. This accelerates interfacial charge transfer, improves electrical conductivity, and reduces the ΔG_{H^*} of the catalyst. Our results signify a modest advancement in the fundamental exploration of HER catalysts. Furthermore, these results hold great potential in the development of high-performance and low-cost industrial milestone catalysts.

ACKNOWLEDGMENTS

This study was supported by the National Research Foundation of Korea (NRF-2021R1A2C4001777, NRF-2022M3H4A1A04096482 and RS-2023-00229679), the National Natural Science Foundation of China (No. 21965005, 52363028), the Natural Science Foundation of Guangxi Province (2021GXNSFAA076001), and the Guangxi Technology Base and Talent Subject (GUIKE AD20297039). The authors also acknowledge technical support from the 1D beamline (KIST-PAL XRS/XAFS) of the Pohang Light Source-II (PLS-II) in the Pohang Accelerator Laboratory (PAL). B.Z. and L. X. contributed equally to this work.

CONFLICT OF INTEREST STATEMENT

The authors declare that there are no conflict of interests.

ORCID

Hyung Mo Jeong http://orcid.org/0000-0001-5950-3890

REFERENCES

1. Tang K, Hu H, Xiong Y, et al. Hydrophobization engineering of the air-cathode catalyst for improved oxygen diffusion towards efficient zinc-air batteries. *Angew Chem Int Ed*. 2022;61(24):e202202671.
2. Li Y, Peng C-K, Hu H, et al. Interstitial boron-triggered electron-deficient O_s aerogels for enhanced pH-universal hydrogen evolution. *Nat Commun*. 2022;13:1143.
3. Qian Y, Yu J, Lyu Z, et al. Durable hierarchical phosphorus-doped biphase MoS_2 electrocatalysts with enhanced H* adsorption. *Carbon Energy*. 2023:e376. doi:10.1002/cey1002.1376
4. Wang H, Chen Z, Wu D, et al. Significantly enhanced overall water splitting performance by partial oxidation of Ir through Au modification in core–shell alloy structure. *J Am Chem Soc*. 2021;143(12):4639-4645.

5. Peng W, Deshmukh A, Chen N, et al. Deciphering the dynamic structure evolution of Fe- and Ni-codoped CoS_2 for enhanced water oxidation. *ACS Catal*. 2022;12(7):3743-3751.
6. Mahmood J, Li F, Jung S-M, et al. An efficient and pH-universal ruthenium-based catalyst for the hydrogen evolution reaction. *Nat Nanotechnol*. 2017;12(5):441-446.
7. Lu Y, Yue C, Li Y, et al. Atomically dispersed Ni on Mo_2C embedded in N, P co-doped carbon derived from polyoxometalate supramolecule for high-efficiency hydrogen evolution electrocatalysis. *Appl Catal B*. 2021;296(5):120336.
8. Kwon H, Bae D, Won D, et al. Nanoporous silver telluride for active hydrogen evolution. *ACS Nano*. 2021;15(4):6540-6550.
9. Ding K, Hu J, Jin W, et al. Dianion induced electron delocalization of trifunctional electrocatalysts for rechargeable Zn–air batteries and self-powered water splitting. *Adv Funct Mater*. 2022;32(29):2201944.
10. Lai Z, Chaturvedi A, Wang Y, et al. Preparation of 1T′-phase $ReS_{2x}Se_{2(1-x)}$ ($x = 0$–1) nanodots for highly efficient electrocatalytic hydrogen evolution reaction. *J Am Chem Soc*. 2018;140(27):8563-8568.
11. He J, Bhargav A, Yaghoobnejad Asl H, Chen Y, Manthiram A. 1T′-ReS_2 nanosheets in situ grown on carbon nanotubes as a highly efficient polysulfide electrocatalyst for stable Li–S batteries. *Adv Energy Mater*. 2020;10(23):2001017.
12. Wang J, He J, Omololu Odunmbaku G, et al. Regulating the electronic structure of ReS_2 by Mo doping for electrocatalysis and lithium storage. *Chem Eng J*. 2021;414:128811.
13. Liu D, Hong J, Li X, et al. Synthesis of 2H-1T′ WS_2-ReS_2 heterophase structures with atomically sharp interface via hydrogen-triggered one-pot growth. *Adv Funct Mater*. 2020;30(16):1910169.
14. Zhao G, Xia L, Cui P, et al. Atomic-level modulation of the interface chemistry of platinum–nickel oxide toward enhanced hydrogen electrocatalysis kinetics. *Nano Lett*. 2021;21(11):4845-4852.
15. Zhao X, Liu M, Wang Y, et al. Designing a built-in electric field for efficient energy electrocatalysis. *ACS Nano*. 2022;16(12):19959-19979.
16. Sun W-J, Ji H-Q, Li L-X, et al. Built-in electric field triggered interfacial accumulation effect for efficient nitrate removal at ultra-low concentration and electroreduction to ammonia. *Angew Chem Int Ed*. 2021;60(42):22933-22939.
17. Zhai L, She X, Zhuang L, et al. Modulating built-in electric field via variable oxygen affinity for robust hydrogen evolution reaction in neutral media. *Angew Chem Int Ed*. 2022;61(14):e202116057.
18. Li J, Tan Y, Zhang M, et al. Boosting electrocatalytic activity of Ru for acidic hydrogen evolution through hydrogen spillover strategy. *ACS Energy Lett*. 2022;7(4):1330-1337.
19. Xie C, Yan D, Li H, et al. Defect chemistry in heterogeneous catalysis: recognition, understanding, and utilization. *ACS Catal*. 2020;10(19):11082-11098.
20. Mukherjee S, Banwait A, Grixti S, Koratkar N, Singh CV. Adsorption and diffusion of lithium and sodium on defective rhenium disulfide: a first principles study. *ACS Appl Mater Interfaces*. 2018;10(6):5373-5384.
21. Li L, Qin Z, Ries L, et al. Role of sulfur vacancies and undercoordinated Mo regions in MoS_2 nanosheets toward the evolution of hydrogen. *ACS Nano*. 2019;13(6):6824-6834.
22. Wang B, Huang H, Sun T, et al. Dissolution reconstruction of electron-transfer enhanced hierarchical NiS_x-MoO_2 nanosponges as a promising industrialized hydrogen evolution catalyst beyond Pt/C. *J Colloid Interface Sci*. 2020;567:339-346.
23. Nguyen DA, Jo Y, Tran TU, Jeong MS, Kim H, Im H. Electrically and optically controllable p–n junction memtransistor based on an Al_2O_3 encapsulated 2D Te/ReS_2 van der Waals heterostructure. *Small Methods*. 2021;5(12):2101303.
24. Tongay S, Sahin H, Ko C, et al. Monolayer behaviour in bulk ReS_2 due to electronic and vibrational decoupling. *Nat Commun*. 2014;5:3252.
25. Xu J, Shao G, Tang X, et al. Frenkel-defected monolayer MoS_2 catalysts for efficient hydrogen evolution. *Nat Commun*. 2022;13:2193.
26. Zheng X-Y, Yao C-B, Li H-Y, et al. Excitonic effects in the linear and nonlinear optical response of rhenium disulfide regulated by Re vacancy. *Adv Opt Mater*. 2023;11(10):2202871.
27. Xia L, Jiang W, Hartmann H, Mayer J, Lehnert W, Shviro M. Multistep sulfur leaching for the development of a highly efficient and stable NiS_x/$Ni(OH)_2$/NiOOH electrocatalyst for anion exchange membrane water electrolysis. *ACS Appl Mater Interfaces*. 2022;14(17):19397-19408.
28. Xu X, Zhao H, Wang R, et al. Identification of few-layer ReS_2 as photo-electro integrated catalyst for hydrogen evolution. *Nano Energy*. 2018;48:337-344.
29. Lin J, Wang P, Wang H, et al. Defect-rich heterogeneous MoS_2/NiS_2 nanosheets electrocatalysts for efficient overall water splitting. *Adv Sci*. 2019;6(14):1900246.
30. Lei X, Tang Q, Zheng Y, et al. High-entropy single-atom activated carbon catalysts for sustainable oxygen electrocatalysis. *Nat Sustain*. 2023;6(7):816-826.
31. Jajko G, Gutiérrez-Sevillano JJ, Sławek A, et al. Water adsorption in ideal and defective UiO-66 structures. *Microporous Mesoporous Mater*. 2022;330:111555.
32. Li Z, Xiao C, Fan S, et al. Dual vacancies: an effective strategy realizing synergistic optimization of thermoelectric property in BiCuSeO. *J Am Chem Soc*. 2015;137(20):6587-6593.
33. Guo N, Xue H, Bao A, et al. Achieving superior electrocatalytic performance by surface copper vacancy defects during electrochemical etching process. *Angew Chem Int Ed*. 2020;59(33):13778-13784.
34. Sun J, Xue H, Guo N, et al. Synergetic metal defect and surface chemical reconstruction into $NiCo_2S_4$/ZnS heterojunction to achieve outstanding oxygen evolution performance. *Angew Chem Int Ed*. 2021;60(35):19435-19441.
35. Yang Y, Kang Y, Zhao H, et al. An interfacial electron transfer on tetrahedral NiS_2/$NiSe_2$ heterocages with dual-phase synergy for efficiently triggering the oxygen evolution reaction. *Small*. 2020;16(1):1905083.
36. Tan L, Yu J, Wang C, et al. Partial sulfidation strategy to NiFe-LDH@$FeNi_2S_4$ heterostructure enable high-performance water/seawater oxidation. *Adv Funct Mater*. 2022;32(29):2200951.
37. Huang J, Gao H, Xia Y, et al. Enhanced photoelectrochemical performance of defect-rich ReS_2 nanosheets in visible-light assisted hydrogen generation. *Nano Energy*. 2018;46:305-313.
38. Feng Q, Li M, Wang T, et al. Low-temperature growth of three dimensional ReS_2/ReO_2 metal-semiconductor heterojunctions on graphene/polyimide film for enhanced hydrogen evolution reaction. *Appl Catal B*. 2020;271(15):118924.

39. Qian Y, Yu J, Zhang F, Kang Y, Su C, Pang H. Facile synthesis of sub-10 nm ZnS/ZnO nanoflakes for high-performance flexible triboelectric nanogenerators. *Nano Energy*. 2021; 88:106256.
40. Jia X, Kang H, Yang X, et al. Amorphous Ni(III)-based sulfides as bifunctional water and urea oxidation anode electrocatalysts for hydrogen generation from urea-containing water. *Appl Catal B*. 2022;312(5):121389.
41. Wang B, Huang H, Huang M, Yan P, Isimjan TT, Yang X. Electron-transfer enhanced MoO_2-Ni heterostructures as a highly efficient pH-universal catalyst for hydrogen evolution. *Science China Chemistry*. 2020;63(6):841-849.
42. Ge J, Zhang D, Qin Y, et al. Dual-metallic single Ru and Ni atoms decoration of MoS_2 for high-efficiency hydrogen production. *Appl Catal B*. 2021;298(5):120557.
43. Li Q, Wang D, Han C, et al. Construction of amorphous interface in an interwoven NiS/NiS_2 structure for enhanced overall water splitting. *J Mater Chem A*. 2018;6(18):8233-8237.
44. Wang Q, Xu C-Q, Liu W, et al. Coordination engineering of iridium nanocluster bifunctional electrocatalyst for highly efficient and pH-universal overall water splitting. *Nat Commun*. 2020;11:4246.
45. Qian Y, Yu J, Zhang Y, et al. Interfacial microenvironment modulation enhancing catalytic kinetics of binary metal sulfides heterostructures for advanced water splitting electrocatalysts. *Small Methods*. 2022;6(1):2101186.
46. Yin J, Jin J, Zhang H, et al. Atomic arrangement in metal-doped NiS_2 boosts the hydrogen evolution reaction in alkaline media. *Angew Chem Int Ed*. 2019;58(51):18676-18682.
47. Yang W, Dong L, Yang W, Xu C, Shao G, Wang G. 3D oxygen-defective potassium vanadate/carbon nanoribbon networks as high-performance cathodes for aqueous zinc-ion batteries. *Small Methods*. 2020;4(1):1900670.
48. Chung DY, Lopes PP, Farinazzo Bergamo Dias Martins P, et al. Dynamic stability of active sites in hydr(oxy)oxides for the oxygen evolution reaction. *Nat Energy*. 2020;5(3):222-230.
49. Sun Y, Xue Z, Liu Q, et al. Modulating electronic structure of metal-organic frameworks by introducing atomically dispersed Ru for efficient hydrogen evolution. *Nat Commun*. 2021;12:1369.
50. Zhou KL, Wang Z, Han CB, et al. Platinum single-atom catalyst coupled with transition metal/metal oxide heterostructure for accelerating alkaline hydrogen evolution reaction. *Nat Commun*. 2021;12:3783.
51. Xu L, Huang W-Q, Hu W, et al. Two-dimensional MoS_2-graphene-based multilayer van der Waals heterostructures: enhanced charge transfer and optical absorption, and electric-field tunable dirac point and band gap. *Chem Mater*. 2017;29(13):5504-5512.
52. Li C, Jang H, Liu S, et al. P and mo dual doped ru ultrasmall nanoclusters embedded in P-doped porous carbon toward efficient hydrogen evolution reaction. *Adv Energy Mater*. 2022;12(23):2200029.
53. Zhang R, Ren X, Hao S, et al. Selective phosphidation: an effective strategy toward CoP/CeO_2 interface engineering for superior alkaline hydrogen evolution electrocatalysis. *J Mater Chem A*. 2018;6(5):1985-1990.
54. Yang N, Tian S, Feng Y, et al. Introducing high-valence iridium single atoms into bimetal phosphides toward high-efficiency oxygen evolution and overall water splitting. *Small*. 2023;19(15):2207253.
55. Su L, Cui X, He T, et al. Surface reconstruction of cobalt phosphide nanosheets by electrochemical activation for enhanced hydrogen evolution in alkaline solution. *Chem Sci*. 2019;10(7):2019-2024.
56. Wang Y, Qian G, Xu Q, et al. Industrially promising IrNi-$FeNi_3$ hybrid nanosheets for overall water splitting catalysis at large current density. *Appl Catal B*. 2021;286(5):119881.
57. Liu C, Qian J, Ye Y, et al. Oxygen evolution reaction over catalytic single-site co in a well-defined brookite TiO_2 nanorod surface. *Nature Catalysis*. 2020;4:36-45.
58. Sun H, Chen L, Lian Y, et al. Topotactically transformed polygonal mesopores on ternary layered double hydroxides exposing under-coordinated metal centers for accelerated water dissociation. *Adv Mater*. 2020;32(52):2006784.
59. Fu Q, Wang X, Han J, et al. Phase-junction electrocatalysts towards enhanced hydrogen evolution reaction in alkaline media. *Angew Chem Int Ed*. 2021;60(1):259-267.
60. Zhou Q, Hao Q, Li Y, et al. Free-standing trimodal porous NiZn intermetallic and Ni heterojunction as highly efficient hydrogen evolution electrocatalyst in the alkaline electrolyte. *Nano Energy*. 2021;89:106402.
61. Luo Q, Zhao Y, Sun L, et al. Interface oxygen vacancy enhanced alkaline hydrogen evolution activity of cobalt-iron phosphide/CeO_2 hollow nanorods. *Chem Eng J*. 2022; 437:135376.
62. Wang H, Xu J, Zhang Q, et al. Super-Hybrid transition metal sulfide nanoarrays of Co_3S_4 nanosheet/P-doped WS_2 nanosheet/Co_9S_8 nanoparticle with Pt-like activities for robust All-pH hydrogen evolution. *Adv Funct Mater*. 2022;32(17):2112362.
63. Zhang N, Hu Y, An L, et al. Surface activation and Ni-S stabilization in NiO/NiS_2 for efficient oxygen evolution reaction. *Angew Chem Int Ed*. 2022;61(35):e202207217.
64. Yu F, Zhou H, Huang Y, et al. High-performance bifunctional porous non-noble metal phosphide catalyst for overall water splitting. *Nat Commun*. 2018;9:2551.

SUPPORTING INFORMATION

Additional supporting information can be found online in the Supporting Information section at the end of this article.

How to cite this article: Wang B, Wang L, Lee JH, Isimjan TT, Jeong HM, Yang X. Enabling built-in electric fields on rhenium-vacancy-rich heterojunction interfaces of transition-metal dichalcogenides for ph-universal efficient hydrogen and electric energy generation. *Carbon Energy*. 2024;e526. doi:10.1002/cey2.526